

1 **A magnetic data correction workflow for sparse, four dimensional data**

2

3 **Alan R.A. Aitken¹, Lara Nigro Ramos¹, Jason L. Roberts², Jamin S. Greenbaum³, Lenneke M.**
4 **Jong², Duncan A. Young³, Donald D. Blankenship³**

5 1 – The School of Earth Sciences, The University of Western Australia, Crawley, Western Australia
6 6009, Australia

7 2 – The Australian Antarctic Division, Kingston, Tasmania 7050, Australia

8 3 – The University of Texas Institute for Geophysics, J.J. Pickle Research Campus, Austin, Texas, USA

9 Corresponding author: Alan Aitken (alan.aitken@uwa.edu.au)

10 **Key Points**

- 11 • A new approach to correcting four dimensional aeromagnetic data is developed and tested
12 with the large-scale ICECAP dataset from East Antarctica
- 13 • Substantial improvements in data quality and reliability are seen and error thresholds are
14 well defined.
- 15 • These improvements in data quality support the investigation of subglacial geology and
16 tectonics in magnetic data.

17 **Abstract**

18 High-quality aeromagnetic data are important in guiding new knowledge of the solid earth in frontier
19 regions, such as Antarctica, where these data are often among the first data collected. The
20 difficulties of data collection in remote regions often lead to less than ideal data collection, leading
21 to data that are sparse and four-dimensional in nature. Standard aeromagnetic data collection
22 procedures are optimised for the (nearly) 2D data that are collected in industry-standard surveys. In
23 this work we define and apply a robust magnetic data correction approach that is optimised to these
24 four dimensional data. Data are corrected in three phases, first with operations on point data,
25 correcting for spatio-temporal geomagnetic conditions, then operations on line data, adjusting for
26 elevation differences along and between lines and finally a line-based levelling approach to bring
27 lines into agreement while preserving data integrity. For a large-scale East Antarctic survey, the
28 overall median cross-tie error reduction error reduction is 93%, reaching a final median error of 5 nT.
29 Error reduction is are spread evenly between phase 1 and phase 3 levelling operations. Phase 2 does
30 not reduce error directly but permits a stronger error reduction in phase 3. Residual errors are
31 attributed to limitations in the ability to model 4D geomagnetic conditions and also some limitations
32 of the inversion process used in phase 2. Data have improved utility for geological interpretation and
33 modelling, in particular quantitative approaches, which are enabled with less bias and more
34 confidence.

35 **Plain Language Summary**

36 Observations of the Earth's magnetic field underpin our knowledge of geology and tectonics, and are
37 often among the first data collected in frontier regions. This work focuses on the problems
38 experienced in remote surveys, including observation periods extending over years, and flying
39 heights that vary over kilometres. Conventional approaches are designed for more tightly
40 constrained survey collection and can be inappropriate for these data. A new way to process
41 airborne observations of magnetic field intensity is developed and tested. Applied to a dataset in
42 East Antarctica, the data quality is substantially improved and the data better reveals the geology
43 hidden beneath the ice of Antarctica.

44 **Index Terms**

45 0925, 0910, 0903

46 **1 Introduction**

47 Since the beginnings of plate tectonic theory, observations of the Earth's magnetic field have been
48 essential to understanding the structure and evolution of both continents and oceans [*Behrendt and*
49 *Watorson, 1970; Vine and Matthews, 1963*]. Commonly, magnetic data is one of the first geophysical
50 data sets collected, forming the basis for subsequent investigations of the solid earth with other
51 techniques. Good quality data is essential for the robust interpretation of tectonic systems, including
52 the identification of major tectonic structures, and the internal structuring of tectonic domains, the
53 definition of sedimentary basins, and clear mapping of magnetic polarity reversals in the oceanic
54 crust.

55 In many parts of the world, in particular in regions with resource exploration activity, magnetic data
56 have been systematically collected in regular surveys [*Nabighian et al., 2005*]. High Resolution
57 Aeromagnetic (HRAM) Data is collected at low-flying heights, often < 100m, consistently draped over
58 topography and with individual surveys occurring over a short time period. Lines are arranged in
59 parallel arrays, with spacings often < 1 km. For these surveys, robust data processing workflows

60 exist, being well suited to the survey design and goals typically resulting in a representative data-grid
61 [Nabighian *et al.*, 2005]. Either the line data or the grid can then be interpreted and modelled to
62 provide knowledge of the solid Earth.

63 In other parts of the world, for example in frontier regions, data like these are not widely available
64 either due to a lack of surveying or due to data being proprietary, and the only data available are
65 often from large-scale reconnaissance surveys. These regions are where we, in general, know least
66 about the magnetic structure of the solid earth, and so there is a need to maximise the value of
67 these surveys. Datasets in these regions are defined, overall, by more irregular line directions and
68 spacings, very variable flying heights and terrain separations and by much longer time-frames of
69 data collection.

70 One such region is Antarctica, where data-coverage has been accumulated over decades through
71 many airborne and marine surveys [Chiappini *et al.*, 2002; A. Golynsky *et al.*, 2013; Alexander
72 Golynsky *et al.*, 2006; A V Golynsky *et al.*, 2018; Kim *et al.*, 2007]. Given the lack of outcrop
73 information in Antarctica, these data provide a crucial resource to the understanding of the
74 continental interior, including important aspects such as defining the locations of major tectonic
75 structures [A. R. A. Aitken *et al.*, 2014; Ferraccioli *et al.*, 2011; Tinto *et al.*, 2019], defining
76 sedimentary basins [A. R. A. Aitken *et al.*, 2014; Ferraccioli *et al.*, 2009a; Frederick *et al.*, 2016; Tinto
77 *et al.*, 2019] and mapping major magmatic suites [Behrendt *et al.*, 1996; Ferraccioli *et al.*, 2009b].
78 The knowledge gained from these surveys is often critical for understanding the tectonics of
79 Gondwana and earlier supercontinents [A. R. A. Aitken *et al.*, 2016; Jordan *et al.*, 2017; Ruppel *et al.*,
80 2018], as well as understanding the conditions at the base of the Antarctic Ice Sheet, in particular
81 geothermal heat flux [Martos *et al.*, 2018].

82 Many airborne geophysical data surveys in Antarctica have a sparse and sometimes irregular data
83 distribution, with data collection at a variety of flying heights and over longer time periods than a
84 typical exploration-focused survey, often across multiple field seasons, and sometimes with multiple
85 aircraft and instrumentation suites. Antarctic survey grids, in most cases, have line-spacings of 5 km
86 or more and may be considered sparse, in the sense that the line spacing is typically greater than the
87 source-sensor separation, leading to aliasing in the survey data, at least in the across-line direction
88 [Reid, 1980]. Additional complications include logistical considerations surrounding the cost and
89 complexity of installing remote camps, which promotes the collection of data in long flights
90 undertaken from the widely separated permanent research stations. As a consequence, the survey
91 may occur well away from supporting infrastructure, notably geomagnetic base stations (Fig. 1). In
92 addition, as flight-time increases, regular aligned grids with close spacings become logistically
93 infeasible. The survey may also traverse changing geomagnetic conditions over these long distances
94 and long flight times, with little opportunity to provide cross-validation. The magnetic-polar location
95 is a particularly challenging environment, exacerbated by the inability often to schedule flights
96 explicitly in quiet geomagnetic conditions [Damaske, 1989; Saltus and Kucks, 1995]. Finally, the need
97 to combine multiple forms of data in one platform (often, surface mapping lidar, ice penetrating
98 radar, gravity and magnetic data) leads to further compromises in flight-design and collection
99 procedures. These data are not well-suited to conventional data processing approaches, and a
100 different approach is necessary to generate representative data products, and to maximise benefit
101 to interpretation.

102 In this paper a data correction workflow is developed and tested, seeking to tackle the specific
103 challenges of sparse and four dimensional data. The aim is to reduce, as far as possible, physically
104 predictable spatio-temporal influences on the data before more pragmatic data adjustment
105 procedures are applied. In particular, with a sparse 4D survey, the assumed inter-line relationships

106 that underpin intersection-based or neighbour-based levelling are not necessarily valid. Finally, we
107 seek a workflow that has minimal human data-value decisions, that is largely automated and that
108 can accommodate new data being added with minimal re-adjustment to existing data. This allows
109 an update at the end of each campaign, or in the case of a compilation such as ADMAP, updating as
110 new surveys are added to the database. We apply this approach to a major airborne magnetic
111 dataset from Antarctica, ICECAP [A. R. A. Aitken et al., 2014; Blankenship et al., 2011, updated 2013],
112 which typifies the problems listed above.

113 A particular consideration is to maximise the value of these data for subsurface geological
114 interpretation and modelling to contribute knowledge of subglacial geology. Applications in
115 Antarctica include constraining knowledge of past and current ice sheet states, and in particular to
116 enable the mapping of sedimentary basins [A. R. A. Aitken et al., 2014; Ferraccioli et al., 2009a], sub-
117 ice-shelf cavities and lakes [Greenbaum et al., 2015; Tinto et al., 2019], and the identification of
118 potentially high heat flux areas [Carson et al., 2014; Martos et al., 2018].

119 **2 ICECAP data**

120 The ICECAP data used here span surveys conducted in two multi-year stages. The first stage (ICECAP-
121 I) includes campaigns from the 2008-2009 season to the 2012-2013 season [Blankenship et al., 2011,
122 updated 2013], and were previously published in Aitken et al [2014] and included in the most recent
123 ADMAP-2 compilation [A V Golynsky et al., 2018]. The second stage (ICECAP-II) includes here the
124 data from campaigns in the 2015-16 and 2016-2017 seasons [Roberts et al., 2018]. These were not
125 included in the most recent ADMAP-2 compilation [A V Golynsky et al., 2018]. Earlier ICECAP-I data
126 processing focused on deriving an interpretable image, and included conventional steps such as
127 base-station correction, removal of the International Geomagnetic Reference Field (IGRF) and
128 intersection-based levelling [A. R. A. Aitken et al., 2014].

129 All data collection was undertaken from a Basler BT-67 aircraft, registered C-GJKB, owned and
130 operated by Kenn Borek Air, Ltd. A Geometrics 823A Caesium Vapour magnetometer was mounted
131 in a tail boom, while positioning is provided from central, tail and wingtip mounted GPS sensors.
132 Surface elevation data and ice thickness data was generated from UTIG HiCARS and HiCARS-2 ice
133 penetrating radar systems [Blankenship et al., 2012, updated 2013a]. The surface elevation data was
134 supplemented by Riegl laser-altimeter data [Blankenship et al., 2012, updated 2013b]. Survey
135 priorities were different in different seasons, with initially the focus on large-scale coverage through
136 long radial lines, then subsequently a focus on coastal regions in more conventional grid patterns
137 (Fig. 1). Throughout the program satellite-tracks were flown, also older traverse lines, as well as
138 transit flights and line re-flights. In the data-sparse environment of Antarctica, all these ancillary
139 flights are important to improve coverage.

140 **3 Correction Workflow**

141 The characteristics discussed above lead to a complex data-processing environment demanding, as a
142 particular limitation beyond those of more typical data, the reconciliation of data from different
143 years, different flight heights, different line orientations, at large distances from base stations, and
144 with varying geomagnetic field conditions. Initial data for this study is the raw data with only basic
145 field QC procedures applied [Blankenship et al., 2011, updated 2013; Roberts et al., 2018].

146 The new processing workflow presented here comprises three phases, each with increasing data-
147 connection (Fig. 2): Phase 1 involves point-by-point operations on individual data points; phase 2
148 includes line-by-line operations on individual lines and phase 3 includes multi-line operations on
149 inter-line relationships.

150 Throughout the workflow, several software packages were used, including Oasis Montaj® for
151 database handling and basic data operations, python, POMME [S. Maus et al., 2010] and escript
152 [Gross et al., 2015]. Only POMME and escript have specific properties, and each is open-source;
153 there is no dependence on proprietary techniques. The new approaches used in this study are
154 described in the supporting information.

155 3.1 Phase 1 – Point-by-point operations

156 These data-processing steps are derived taking into account the large spatial and temporal scale of
157 the dataset covering large distances and multiple years. The large volume of data (203 000 line km)
158 and a desire for consistency and repeatability demanded a semi-automated process with minimal
159 human intervention. Several steps are included in phase 1 – basic QC and denoising, IGRF removal
160 [Thébault et al., 2015], correction of spatio-temporal field variations with POMME [S. Maus et al.,
161 2010], and correction of the residual time-varying field with regional base station data.

162 3.1.1 Methods

163 3.1.1.1 Data import, QC and de-noising

164 All data were imported from native ASCII text formats into databases, and data were checked for
165 obviously erroneous values, NaNs, missing data, and other such problems. These were corrected if
166 possible, or the data omitted from further steps if not feasible. Locally noisy data was accounted for
167 using the fourth difference transform [Hood et al., 1979] applied to the time-series data. In the
168 fourth difference processing, data was excluded where a magnitude threshold (unscaled) of 20 was
169 exceeded. A Dirac delta function of x nT provides a 4th difference magnitude of $6x$, while a Heaviside
170 step function of x nT provides a 4th difference magnitude of $3x$. Correspondingly, the threshold
171 applied will allow single-point “spikes” of up to 3.33 nT and single-interval “steps” of up to 6.67 nT.

172 Following thresholding, an automatic routine was used to correct for minor spikes in the data. The
173 routine looks in the fourth difference transform for a sufficient closeness to the characteristic fourth
174 difference pattern of $0x, +1x, -4x, +6x, -4x, +1x, 0x$, where x is the magnitude of the spike. The need
175 for this correction was identified with a moving window, considering both the numerical defect from
176 this pattern, defined as $|i_{n-2} + i_{n-1}/-4 + i_n/6 + i_{n+1}/-4 + i_{n+2}|$ and the symmetricity observed, defined as
177 $(4 \times |(i_{n+1}-i_{n-1})/((i_{n+1}+i_{n-1})/2)| + |(i_{n+2}-i_{n-2})/((i_{n+2}+i_{n-2})/2)|)/5$. If both defect and symmetry were below a
178 tolerance of 0.5, a correction was applied based on $i_n/6$.

179 A procedure was also run to identify steps based on their own characteristic signature in 4th
180 difference transform, i.e. $0x, 1x, -3x, 3x, -1x, 0x$ where x is a step between stations 3 and 4. Using
181 similar equations as for spikes, the size of the step was recorded, however the removal of steps is
182 more nuanced than spikes, and so they were not corrected for here, but are flagged in the database
183 for potential correction in more detailed future studies.

184 3.1.1.2 POMME Geomagnetic Modelling

185 POMME geomagnetic field models attempt to capture in a spherical harmonic model the Earth’s
186 geomagnetic field from the near surface to elevations of several thousand kilometres [S. Maus et al.,
187 2010]. In contrast to the IGRF/DGRF, which accounts for longer-term and long-wavelength magnetic
188 field variations [Thébault et al., 2015], POMME also includes the capacity to include the core,
189 lithospheric magnetospheric and induced fields on much smaller length scales and shorter
190 timescales [S. Maus et al., 2010]. In this study we used the tenth iteration of the model, POMME-10.
191 This model is based on satellite data from the CHAMP (July 2000 – September 2010), Oersted
192 (January 2010 to June 2014), and Swarm (December 2013 to November 2015) satellite missions. For
193 the IGRF we use the 2015 model (12th generation) [Thébault et al., 2015].

194 The required components for POMME modelling were compiled for each data point. As a minimum,
195 the latitude, longitude and elevation of the data point, and the time of data collection are required.
196 For best results, several model components are needed to describe the state of the magnetosphere
197 [S. Maus et al., 2010]. Interplanetary Magnetic Field (IMF) data indices were obtained from
198 OMNIWEB 1 minute data [King and Papitashvili, 2005], from which the y-component of magnetic
199 flux (IMF-By) was extracted in Geocentric Solar Magnetospheric (GSM) coordinates, sampled 35
200 minutes prior to the data collection time. The merging electric field Em was also derived from
201 OMNIWEB data, sampled 60 minutes prior to data collection time. The time lags accommodate
202 delays in the geomagnetic effects of the solar wind relative to measurements at the bow shock [Lühr
203 and Maus, 2010]. Hourly Est/Ist indices representing the external and internal components of the
204 magnetospheric disturbance magnetic field [Stefan Maus and Weidelt, 2004] were obtained from
205 the NOAA geomagnetism server, and sampled at the data collection time. Finally, to parameterise
206 the effect of solar cycles on the ring current, and associated bias in the Est index the 10.7 centimeter
207 solar flux [Tapping, 2013] was obtained from data collected at the Penticton Observatory, for which
208 we use the 81-day central average of observed solar flux. This was sampled 20 months prior to the
209 data collection date [Lühr and Maus, 2010]. Est/Ist and F10.7 coverage is complete over the survey
210 period, but the OMNIWEB record has some periods lacking data. Gaps in the IMF-By and IMF-Em
211 records of less than 2 hours were interpolated with a maximum entropy prediction algorithm. This
212 approach maintains noise characteristics similar to the original data. Any remaining gaps were
213 assigned default values of 0 for IMF-By and 0.5 for IMF-Em.

214 POMME is used here as an alternative to the IGRF, seeking to improve the representation of higher
215 frequency components of the magnetic field in the data correction process. We visualise this using
216 the long-term record from Scott Base from 2008/07/01 to 2013/06/30 (Fig. 3). Power spectral
217 density for the full POMME correction for this record is similar to the IGRF at frequencies of 1 per 90
218 days or lower, but a substantial difference in power spectral density is seen for higher frequencies.
219 POMME correction with default values for the magnetospheric components (i.e. IMF-By, IMF-Em,
220 Est, Ist and F10.7) matches the IGRF more closely, although providing higher power to diurnal and
221 sub-diurnal cycles. Despite being substantially higher powered than the IGRF, the power spectral
222 density of POMME remains well below the observed signal (Fig. 3).

223 3.1.1.3 Multiple Base Station Correction

224 Following the POMME data correction process, an explicit base-station correction is applied to
225 account for remaining temporal field variations at higher frequencies (Fig. 3). Conventional methods
226 using a local base station directly are not appropriate here, and so we define a method for the use of
227 multiple distant base stations, similar in concept to previous approaches [Abraham et al., 2008]. The
228 method accounts for several influences that are not accounted for in single station base-station
229 procedures. First, it allows for multiple base stations to be included, for this study up to 6; second,
230 the procedure smoothly and automatically transitions between base-stations as the flight-line
231 traverses through space; third, the correction from each station is inverse distance weighted using a
232 power law function, the order of which is able to be specified. Inverse distance weighting is applied
233 relative to a variable scaling-factor dependent on the furthest included station. Observations distant
234 from any station are minimally corrected, reducing the risk of over-correction, while those close to a
235 station, or stations, will receive stronger corrections. The fourth consideration in the correction is
236 the geomagnetic distance, given by the difference in inclination, and the procedure allows to
237 exclude stations that are geomagnetically distant from the observation (e.g. MAW see Fig. 1).
238 Finally, the procedure allows for the vertical damping of base station records, accounting for
239 elevation differences. For this adjustment, a square plate model is used [Telford et al., 1990], with a
240 user-specified width – narrower plates provide stronger vertical damping.

241 Large corrections from distant stations are high risk, potentially causing over-correction, and so as a
242 measure of the risk of over-correction from distant stations the “leverage” applied to the correction
243 is calculated. Leverage is defined for each contributing base station as the magnitude of the station
244 correction multiplied by the distance to that station relative to the length scale. Overall leverage is
245 defined by the sum over all included stations. Leverage may be used to exclude high-risk corrections.

246 3.1.2 Base Station Data Application

247 Base station data are used here for two purposes. First we use the long-term station records for the
248 period from 2008/07/01 to 2013/06/30, covering the ICECAP-I data collection, to test the point-by-
249 point operations for effectiveness. These data also are used to correct the ICECAP-I data, while for
250 ICECAP-II, we obtain the base station data only for the specific data collection periods.

251 Base station data were obtained from the International Real-time Magnetic Observatory Network
252 (INTERMAGNET), with 1-minute sampling interval. The observatories available in the region were,
253 Casey station (CSY), Dome C (DMC) Dumont d’Urville (DRV), Mawson (MAW), Scott Base (SBA) and
254 Vostok (VOS). These six stations circumscribe the survey area (Fig. 1).

255 Of these stations, temporal data coverage is variable: DRV, MAW and SBA have complete long-term
256 records with recovery respectively 99.5%, 99.7% and 99.6%. CSY is very nearly complete, excepting a
257 period with no data for 33 days between 2012/10/09 and 2012/11/11, with 100% recovery during
258 station “on” time. DMC covers the complete period, but with a prolonged period with no data
259 (2009/06/30 to 2010/01/01), and lower recovery overall (96.9%). VOS data is available only from
260 2011/01/01 onwards, but has no data between 2012/12/31 and 2013/05/02. 99.6% recovery is
261 achieved during station “on” time. Consequently CSY, DRV, MAW and SBA are consistently available
262 during ICECAP-I surveying, but DMC and VOS had important drop outs in this time. For the ICECAP-II
263 survey periods, recovery was essentially complete for all stations, with over 99.9% recovery rate
264 during station “on” time. DMC was not operational from 2015/12/28 to 2016/01/07, however.

265 The 4th difference noise reduction measures reduced the bulk long-term noisiness of all stations, as
266 indicated by the standard deviation (Fig. 4). Small reductions are seen at CSY, DMC, VOS and SBA, due
267 to the loss of small amounts of noisy data, < 2%, and only minor corrections applied. DRV and MAW
268 saw larger reductions due to the loss of substantial amounts of data, 12% data loss at MAW and 8%
269 at DRV.

270 For all base station records the correction for POMME predictions sees a reduction in the variability
271 of the signal, but with varying effectiveness (Fig. 4). Only small reductions in variability are seen for
272 DRV of -1.7 nT (3.8%), for DMC of -2.3 nT (5.7%) and for VOS of -2.8 nT (6.5%). For DMC and VOS,
273 this likely reflects their high altitude, whereas the effectiveness of POMME for DRV may be
274 restricted by its position near the pole. Substantially greater variability reductions are seen for MAW
275 of -7.8 nT (16.0%), for CSY of -12.7 nT (23.3%) and for SBA of -37.9 nT (45.1%).

276 Inter-base corrections are not part of the correction workflow for base station data (Fig 2) however
277 we apply this here to the long term data records to establish the effectiveness of the method, and to
278 optimise the parameters. For each base station record, we use low-pass filtered records from the
279 other five stations to correct for residual geomagnetic field variations, especially at higher
280 frequencies. Flight data are situated in between stations, and so this represents a “worst-case”
281 scenario in terms of distances between stations. For the base-station correction, we tested the
282 relative importance of the number of stations to be included, the order of the power law function
283 and the cutoff period for the low pass filter. For all stations except MAW, testing suggests that the
284 optimum variability reduction is made by including the nearest four stations, and by using an inverse

285 distance weighting of order two (inverse distance squared). Filter periods of 30 minutes to 360
286 minutes were tested with the strongest result obtained for a period of 120 minutes. Shorter periods
287 show over correction at CSY and DRV, while longer periods showed under-correction at VOS. These
288 settings were adopted for the field data correction. Vertical damping was found to reduce, to a small
289 extent, the variability at DMC and VOS, suggesting utility for high elevation data, but otherwise was
290 ineffective, and was not used with field data. Corrections using just the nearest single station are
291 markedly inferior at CSY, DRV and SBA, and more mildly inferior at DMC, VOS and MAW (Fig 4).

292 Relative to the POMME-corrected data, substantial reductions in variability are made for VOS of -
293 12.7 nT (31.7%) and for DMC of -8.2 nT (21.6%). These stations are close together, and have similar
294 geomagnetic characteristics. Smaller variability reductions are made for SBA of -4.8 nT (10.4%), DRV
295 of -2.5 nT (5.8%) and CSY, of -0.1 nT (0.2%). Mawson is magnetically, and spatially, quite distant from
296 the other stations, and the base-to base data correction fails for this station, with an increase in
297 variability of 7.2 nT (17.6%). As a consequence of this poor result, for the field data correction, we
298 set the maximum geomagnetic inclination difference at 10°; this value excludes all stations but VOS
299 and MAW for data near MAW, while allowing data near DRV to receive corrections from CSY, DMC
300 and SBA.

301 3.1.3 Field Data Application

302 As with base station data, flight-line data were checked for obviously erroneous values, location or
303 time-tagging issues, NaNs, missing data, cultural effects and other such problems that were
304 corrected if possible, with the data omitted from further steps if not feasible. The same fourth
305 difference processing was applied to flight lines, first with a threshold of 20 to remove noisy data,
306 and despiking, with steps identified but not removed automatically. Very few data were altered as a
307 consequence of this process, and so all subsequent steps used the whole dataset, retaining the
308 potential to mask the results according to these thresholds.

309 For field data, we must also allow for changes in spatial location as well as time. The POMME model
310 resolves spatio-temporal variations in the magnetic field, including some of the lithospheric signal
311 that we wish to retain. Therefore, to appropriately reduce the field data, we apply a correction that
312 reduces our data to the IGRF-reduced data standard at a particular time, t_0 , in this case the 1st of
313 January 2010.

314 The first step is to remove the IGRF, which we calculate for each data point at time t_0 , using the 12th
315 generation model [Thébault *et al.*, 2015] for all data locations. This accounts only for the spatial
316 variations in the geomagnetic field. Spatio-temporal variations from this standard are defined using
317 POMME. We calculate the full POMME correction at the time of data collection, t_t , and also at the
318 reference time, t_0 . The difference between these provides an additional spatio-temporal
319 geomagnetic correction for each data point, so removing temporal differences in the main field,
320 magnetospheric and lithospheric components. The magnitude of these corrections may be
321 substantial, up to 211.5 nT, with a mean of 41.6 nT, a median of 18.3 nT, and root-mean-square
322 (RMS) of 62.7 nT for the ICECAP data.

323 Base-station corrections were applied to each field data-point using up to 4 base stations, with an
324 inverse-distance-squared weighting, and without any vertical damping. Prior to field-data correction
325 the observatory records were corrected for POMME variations, demeaned and low-pass filtered with
326 a minimum period of 120 minutes (Fig 2). The maximum geomagnetic distance permitted was an
327 inclination difference of 10°, a little less than the difference between VOS and DRV (11.8°). As with
328 the POMME correction, the magnitude of these corrections may be substantial, up to 277.0 nT, with
329 a mean of 40.6 nT, a median of 29.7 nT, and RMS of 55.3 nT.

330 An evaluation of the merit of these data reductions can be made through analysis of residual cross-
331 tie errors. In doing so it must be borne in mind that the survey is four-dimensional. Time differences
332 associated with line intersections vary from several hours to several years, while elevation
333 differences vary from a few metres to over 1 km. The majority of the intersections come from the
334 denser surveys near the coast, therefore, intersection-based measures are not fully representative
335 of the magnitude of error, nor its reduction, much of which occurs in the more remote areas with
336 few line-intersections.

337 Cross-tie errors for the raw TMI data are up to 1325.1 nT, with an RMS error of 120.1 nT, a mean
338 error of 90.9 nT and a median error of 71.4 nT (Fig. 5). As expected, the IGRF correction for spatial
339 variation alone yields very little change to these values. On application of the spatio-temporal
340 POMME correction, the maximum cross-tie error is unchanged, however the RMS, mean and median
341 values are all reduced, to 101.7 nT, 75.1 nT and 56.7 nT respectively. In terms of RMS, this is a
342 reduction of 15% from the raw data. Applying the base-station correction reduces cross-tie errors
343 further, with the RMS reduced to 77.4 nT, the mean to 54.7 nT and the median to 38.2 nT. Overall,
344 Phase-1 of data correction has reduced the cross-tie errors by approximately ~40%.

345 3.2 Phase 2 – Line-by-line operations - Elevation Adjustment

346 In phase 2, we seek to adjust for another major variable in the data, which is differential flying
347 heights between lines. For ICECAP data, the data are collected at WGS84 ellipsoidal elevations
348 varying from -43 m to 4199 m. Most of this is dictated by the presence of the ice sheet, but
349 occasionally differences are due to operational requirements. Source-to-sensor separation distance
350 is therefore highly varied, both between lines and also along lines, with as much as 5 km variation
351 being seen on individual lines (e.g. Fig. 6). A common approach to mitigate this is to apply either
352 field continuation or equivalent source methods [*Pilkington and Boulanger, 2017*]. Commonly used
353 FFT-based techniques assume evenly-spaced data collection on a level 2D plane (or 1D line) and are
354 not strictly valid for drape-to-level or drape-to-drape corrections, and their use can introduce
355 substantial errors [*Phillips, 1996*].

356 An alternative to field continuation is to use an equivalent source method, through the generation of
357 magnetic sources at the Earth surface to indirectly define the observed magnetic field, which can
358 then be recomputed on another surface [*Pilkington and Boulanger, 2017*]. A variant of this is to
359 pursue correction through inversion techniques, which allows for a more nuanced definition of the
360 source, including sources that are extensive at depth, and have 3D geometries. Furthermore,
361 modern inversion tools are optimised to deal with large datasets on HPC infrastructure and, while
362 more computationally expensive, can provide stable results in a time-efficient manner. In this case
363 we apply an inversion technique, applied using the open-source package *escript* [*Gross et al., 2015*].

364 3.2.1 Method

365 *escript* solves the inversion problem using the finite element method. *escript* has several capabilities
366 that lend itself to our purpose: First, the magnetic field is a continuous function, piecewise-defined,
367 everywhere within the inversion domain. Consequently, with a single inversion run, multiple data-
368 realisations can be derived, both above and below the original flight height, without any
369 recomputation. For example, we may sample the calculated magnetic field at constant altitudes, or
370 as “draped” surveys at various heights above the surface, or on any other geometry we may choose.
371 In this case we analyse only the constant altitude product at 2 km elevation. A second advantage is
372 that the inducing magnetic field may smoothly vary within the domain, and everywhere the correct
373 intensity and field orientation can be used. This is essential for our long lines traversing, in some
374 cases, highly variable geomagnetic conditions. Third, the method allows data lines to be reduced to a

375 consistent data-derived standard of fit. Finally, the method is easily automated and while compute-
376 intensive, can be run as a “set-and-forget” operation on modern HPC infrastructure.

377 The inversion approach operates on each line independently, and is automated. Several steps are
378 undertaken: First the original flight lines, which may be curved, are cut into straight line-segments,
379 permitting not more than a 45° turn over 10 km. Minimum line-segment length is 20 km. For input
380 to inversion, data are reduced to a common sample frequency of 1 Hz (ca. 80-90m at the typical
381 aircraft velocity). The data file provided to the inversion contains the following required information:
382 longitude, latitude, along line distance, flight elevation, bed elevation, magnetic intensity, IGRF field
383 intensity, inclination and declination. These data are derived from ICECAP data re-sampled at the
384 magnetic data points. ICECAP radar data does not everywhere resolve bed topography, for example
385 due to very deep ice, subglacial lakes and ice shelf cavities, and we fill data gaps with the
386 BedMachine Antarctica model [Morlighem, 2019.]. escript has capacity for unstructured meshing,
387 promising much reduced computational requirements, however for this work a regular rectilinear
388 domain with cuboidal elements is used, due to easier automation of the domain building process.

389 First, a 3D inversion domain is built from the data file, in data-defined UVW coordinates, applying
390 suitable padding to the ends, top, base and sides of the data extents. In our case we take the line-
391 segment data file and define vertical (W) extents extending 2.5 km above the highest data elevation,
392 and 1 km below the lowest bed elevation. In the along line direction (U), padding is added to each
393 end of the domain of approximately 2 times the domain height, defined as above. The lateral (V)
394 extent of the domain is 5 times the domain height. The element length (ΔU) is set everywhere to the
395 average data-point interval in the data file (typically ca. 80-90 m), while element height (ΔW) is set
396 to 50 m. In the lateral direction, just 7 elements are used, so the element size (ΔY) is much larger.
397 Inversion therefore is essentially of a 2.5D nature [Rasmussen and Pedersen, 1979].

398 Second, the model is populated with the data. Magnetic data are located in the relevant elements,
399 with the data-function defined at element-centroids on the central V-element only. All other
400 functions are continuous functions defined on element nodes, extensive across all V elements. The
401 solid Earth, within which and only within which we wish to permit susceptibility changes, is defined
402 using a fuzzy set approach: First we define the set of elements that are not entirely above the local
403 surface, to which “solid Earth” membership is assigned. Then, we define the set of elements that are
404 not entirely below the surface, to which “not solid Earth” membership is applied. For elements that
405 belong to both sets, we re-assign the solid Earth membership value according to the extent to which
406 the element is occupied by the solid Earth. For example for an element extending from 0 to 50 m, if
407 the surface elevation is 25 m, the solid Earth membership value would be 0.5. The susceptibility
408 response of the model is scaled according to the solid Earth membership function (Fig. 6b). This
409 implementation preserves the volume of the solid earth, but not the shape, so a suitable vertical
410 separation of at least ΔU must be ensured to accommodate the meshing precision.

411 The model domain is also populated with the values of the inducing magnetic field, as described by
412 the IGRF (here calculated at time t_0 , and at the lowest bed-elevation in the input data). The inducing
413 field is piecewise translated into UVW field components, accounting for the line orientation relative
414 to true north (φ_U). φ_U is defined as the arctangent of the longitudinal distance over the latitudinal
415 distance, ensuring quadrant is preserved (numpy.arctan2 function). The orientation is calculated
416 over ten data points (~800-900m in this case). This avoids introducing sharp changes as a
417 consequence of location errors or abrupt deviations from the overall line direction, but
418 accommodates gradual turns and curvatures relative to the direction of true north.

419 To perform the inversion, the built in magnetic intensity inversion module of escript is called, to
420 generate an approximate solution to the susceptibility required in the subsurface to explain the
421 observed magnetic field intensity variations. We apply the inversion as a series of attempts to solve
422 the problem, beginning with a highly regularized (i.e. smooth) solution, and progressively relaxing
423 the regularization until the target RMS misfit is reached, or until a number of cycles have been
424 completed without a suitable result. The trade-off parameter μ describes the relative importance of
425 data fit to smoothness in the inversion cost function, with larger values emphasising data fit [*Gross*
426 *et al.*, 2015].

427 Using the susceptibility solution derived, the associated magnetic field is sampled at the desired
428 locations within the domain. In our case, we consider the field sampled at a constant elevation of
429 2000 m. This realisation gives an elevation adjusted version of the magnetic data, that is, they have
430 been corrected for the varying flight elevation, but still contain topographic effects from variable
431 bed topography. Draped realisations may be derived from the models, however, they are more
432 prone to instability and error from the often highly variable subglacial topography, and the high
433 degree of downward continuation that may be required.

434 The elevation adjustment may involve downward continuation of the survey which may also
435 introduce errors into the data. In contrast to frequency-domain downward continuation, the result
436 of the inversion approach is numerically stable for this adjustment. However, while the amplitudes
437 of existing anomalies will be adjusted, downward-adjusted data will not gain short-wavelength
438 components that may be present in genuine data collected at a lower elevation. Upward adjusted
439 data will lose short wavelength components appropriately.

440 3.2.2 Application

441 963 line-segments were modelled using the Magnus supercomputer, a Cray XC40, located at the
442 Pawsey Supercomputing Centre located in Perth Western Australia. The automated modelling
443 procedure reads the data for an individual line from the overall database output in ASCII txt format,
444 builds a domain and runs an inversion as described above.

445 In our application the target RMS misfit was 3 nT, and the maximum number of cycles permitted was
446 6, each cycle for up to 50 iterations or until convergence is reached. Convergence in escript occurs
447 when the size of the model update from an iteration is below a certain tolerance factor of the overall
448 model size [*Gross et al.*, 2015]; in this case the tolerance factor was $1e^{-4}$. Convergence does not
449 imply a satisfactory result from the point of view of data misfit, therefore, multiple cycles may be
450 needed. Between cycles, the model trade-off parameter, μ , was increased by an order of magnitude,
451 beginning at $1e^{-1}$ up to a maximum of $1e^4$. At the conclusion of each cycle the model process was
452 terminated, if RMS misfit was satisfactory, or if not, the results were passed into the next cycle.

453 Of the 963 line-segments, 893 satisfactorily reduced RMS misfit to less than 3 nT within 6 cycles. All
454 but 13 lines had residual RMS misfits of less than 10 nT and the worst residual misfit was 29.9 nT.
455 The elevation adjustments made were substantial. Adjustment to a constant elevation of 2000 m
456 involved magnitudes up to 1981.6 nT, with a mean of 22.4 nT, a median of 11.9 nT, and RMS of 41.3
457 nT. Despite the substantial changes in magnetic field, there was little direct impact on misfit-
458 reduction (Fig. 5).

459 Individual jobs used between one and twelve 24-cpu compute nodes, running for periods up to
460 several hours. As an example, ASB_JKB0a_GL0211a, a large line with 8900 data points, was
461 completed on 5 nodes in 3 hrs and 42 minutes, consuming 445 cpu-hours to achieve a final RMS
462 misfit of 0.89 nT after 4 cycles of iterations. A shorter line, TOT_JKB2n_Y15b, with 1272 data points,

463 was completed on 1 node in 52 minutes, consuming 21 cpu-hours to achieve a final RMS misfit of
464 2.22 nT after 3 cycles of iterations. Model run-time varied with the number of data points, coupled
465 with the complexity of the magnetic field and subglacial topography.

466 3.3 Phase 3 – Multi-line operations - Levelling

467 Following these corrections, the overall cross-tie errors have been reduced by ~40%. In the final
468 phase, we apply a two-stage levelling process to account for residual errors following these
469 corrections. Unlike an HRAM survey, line-intersections in this data are associated with large
470 differences in time and elevation. Although these differences are adjusted for, we may consider
471 levelling in this case as an attempt to bring independent data into mutual agreement, rather than a
472 correction as such. Implicitly, preserving the data integrity along the line is more important than
473 ensuring a low crossover error with other lines. Therefore we apply a conservative line-based
474 approach, comprising first a base-level adjustment (DC shift), and second spline-based levelling.
475 Levelling is applied to both the corrected TMI data and to the data adjusted to an elevation of 2000
476 m.

477 3.3.1 Method

478 The ICECAP data do not everywhere possess a clear hierarchy or ordering of the line sets. Although
479 many of the sub-surveys are flown with distinct orthogonal line sets, these are not well aligned with
480 each other, and furthermore they overlap and are intersected by regional lines of a variety of
481 orientations. Therefore inevitable problems emerge with respect to structuring the levelling
482 approach. Two fundamental choices exist, being network-adjustment methods focusing on loop-
483 closures, or line-based levelling using smooth functions which we use here.

484 3.3.1.1 Median Line Levelling

485 In the first stage, we seek to apply only a base-level adjustment to each line. With the ICECAP data,
486 which has no particular line hierarchy, we must first define the hierarchy of lines, to specify the
487 order of correction. A customised technique is developed, using the median cross-tie error on each
488 line as representative of the adjustment needed.

489 Line-segment intersections are defined by cycling through line-segment pairs, and for each linear
490 line-segment, recording the points on the target line-segment that are within 50 m of a point on the
491 reference line-segments. With the linear line-segments, multiple crossings are not possible, and so
492 for each line-segment pair, we seek one value that defines the cross-tie error, recording for the
493 target line the point location, FID and the value adjustment required to match the reference line.

494 Our approach to levelling these lines uses the median cross-tie error from the intersection points to
495 define the optimal correction for each line-segment. It may be the case, due to oblique intersections
496 or where lines are coincident, that more than one point is returned as an intersection for any given
497 line-segment pair. In this case the mean cross-tie error of the intersection points is assigned to the
498 mean XY location of the intersection points, and so only one value is given for each line-segment
499 pair.

500 Adjustments are applied in an iterative fashion. In the algorithm, the line-segments are ordered in
501 “worst-first” order, based on the median cross-tie error for each line-segment. The algorithm adjusts
502 the worst line-segment, and updates all the cross-ties on applicable reference lines. The algorithm
503 then adjusts the second worst line and so on until all lines have been adjusted. Several iterations of
504 this cycle are repeated, testing for convergence to a given standard, defined by the reduction of the
505 highest line-segment median to a given value. The final adjustments are applied line-by-line to the
506 data.

507 3.3.1.2 Spline-based Levelling

508 Following the median based line-levelling, the data set is able to be addressed with spline-levelling
509 techniques. In practice, the optimum levelling approach at this stage depends on the desired
510 application and target region. For this study we apply a conservative spline-levelling approach that is
511 appropriate for application to the entire dataset. For each line-segment, the residual cross-tie errors
512 after median-based levelling are calculated. Tie-points based on more than 5 reference points are
513 excluded to eliminate highly oblique intersections, and the remainder are halved so as to factor in
514 the corresponding adjustment to the reference line. A tensioned spline is fitted through these
515 points, and the second derivative of the spline is calculated. For each line we apply an iterative
516 procedure to remove points associated with high curvature: Each iteration removes the highest and
517 lowest curvature points, if they also exceed a specified threshold. This process avoids human
518 decisions over line-segment hierarchy and data value, and avoids over-correction of the data, at the
519 cost of a systematic under correction. Residual errors may be dealt with manually for specific areas.

520 3.3.2 Application

521 For both the corrected TMI data and the elevation adjusted data, median-based levelling was
522 applied to the 963 line-segments, for which 9,488 line-segment pairs were identified. 58 line-
523 segments did not possess any intersections and are excluded. The levelling algorithm was applied
524 with a desired standard of 1 nT and a maximum number of cycles of 20. For both the corrected TMI
525 and elevation-adjusted TMI, convergence was achieved to the data standard before 20 cycles were
526 completed. Post-correction, a further 45 line-segments were excluded due to visible line-correlated
527 effects, lack of suitable cross-ties or erroneous values. Excluded line-segments were not levelled
528 using the intersection values, but were brought into agreement with the rest of the data by applying
529 a base-level adjustment derived from the mis-match of the data to a low-resolution (20 km) regional
530 grid of the retained lines, after levelling.

531 Median-based line levelling is a powerful component of the correction process, resulting in
532 substantial changes to the data (see supporting information), and the expected reduction in the
533 overall cross-tie error (Fig. 5). For the corrected TMI, the largest adjustment applied through median
534 line levelling was 1300.4 nT, the mean 31.2 nT, the median 17.0 nT and the RMS 42.7 nT. For the
535 elevation adjusted TMI, adjustments were similar being up to 1305.2 nT, with a mean of 34.7 nT, a
536 median of 20.6 nT and an RMS of 57.2 nT. The difference in magnitude occurs due to the de-
537 meaning process applied during the elevation adjustment. The inversion uses de-measured data, after
538 which the mean is returned to the data without back-adjustment. If the elevation adjustment is not
539 zero-mean (Fig. 7), then a base-level error is introduced. The result is that, although cross-tie errors
540 overall slightly increased with elevation adjustment, this is easily corrected for and the elevation
541 adjusted data is substantially more internally consistent once base-level adjustments have been
542 applied (Fig. 5).

543 For each data set, spline levelling was applied with a tension of 1 and a smoothness of 0.7, giving a
544 smooth adjustment overall, with the second derivative not exceeding $2e^{-5}$ nTm⁻². Two ten-iteration
545 cycles of the spline-levelling algorithm were applied, recomputing intersections in between. In the
546 corrected TMI dataset, 17,889 ties were initially available, with the final levelling using 13,950. With
547 the elevation adjusted data, 17,889 ties were available, of which 14,087 were used in the final
548 levelling.

549 For the corrected TMI, the change to the data from the spline-levelling process was less than in all
550 the previous steps, with a maximum adjustment of 203.9 nT, a mean of 11.4 nT, a median of 5.6 nT,
551 and an RMS of 20.5 nT. The residual RMS cross-tie error is reduced to 41.5 nT, the mean to 19.0 nT

552 and the median to 5.9 nT. For the elevation adjusted data, results are similar with a maximum
553 adjustment of 155.7 nT, a mean of 11.4 nT, a median of 5.7 nT, and an RMS of 19.8 nT. The residual
554 RMS cross-tie error is reduced to 29.1 nT, the mean to 14.0 nT and the median to 4.8 nT (Fig. 5).

555 **4 Results**

556 The data processing has generated the corrected TMI at original flight elevation, and an elevation-
557 adjusted dataset at 2000m above the WGS84 ellipsoid (Fig. 8). The latter is the superior product and
558 has brought out many of the higher amplitude features beneath thick ice in the inland region.
559 Similarly, some coastal anomalies are relatively subdued.

560 The elevation adjusted data can more safely be used in mapping, and especially so for any
561 quantitative work that is sensitive to the amplitudes of anomalies, which in previous regional
562 products are inconsistently defined due to differences in flying height [A. R. A. Aitken *et al.*, 2014; A
563 V Golynsky *et al.*, 2018]. For example, in figure 8 (inset) we see more clearly the sub-linear anomalies
564 in the inland region (e.g. *a*), that are now of comparable amplitude to those near the coast (e.g. *b*),
565 suggesting a similar origin. In the corrected TMI the amplitude of these anomalies is lower, leading
566 to the potential for misinterpretation.

567 **5 Discussion**

568 5.1 Utility of the results

569 The final cross-tie errors in general exceed our target of 3 nT, but are within the error threshold of
570 large regional data-grid compilations, when compared with long survey lines [Milligan *et al.*, 2009]
571 and the dataset is adequately precise for most regional investigations. Further adjustment on the
572 basis of line-intersections would of course reduce these errors, but we consider that, due to the
573 incomplete data corrections applied in phase 1 and phase 2, the data remain 4D, and so it is not
574 valuable to pursue an exact fit through levelling.

575 Given the diverse nature of the ICECAP dataset, additional levelling procedures may be fruitful for
576 specific purposes, for example traditional tie-line/flight line levelling can be applied to the high
577 resolution grid-pattern surveys near the coast; while closed-loop methods may be valuable for the
578 moderate-density regions (e.g. inset, Fig. 8). Our data processing provides a regionally consistent
579 starting point for more targeted investigations at smaller scales.

580 The data, in particular the elevation adjusted data, are consistently processed and have a sufficiently
581 small error threshold to be suitable for careful inclusion in automated and quantitative
582 interpretation methods. The data remain aliased in areas with sparse data (e.g. inset, Fig. 8), and this
583 can only properly be rectified by the addition of data. Finally, in the data presented here we do not
584 correct for the shape of the topographic surface, and so there may be residual effects. For example,
585 in figure 8 (inset) the Denman Glacier trough can be seen as a magnetic low, and the Totten and
586 Moscow University ice shelves also have magnetic lows. At least part of this magnetisation deficit
587 may be due to the low topography, however, geological processes, such as faulting or basin
588 formation, are also plausible causes for reduced magnetisation.

589 5.2 Value of the workflow

590 A crucial question is the value of this approach relative to its cost, in comparison to other
591 approaches. For each phase we can define some guidelines as to when this approach is beneficial.
592 We consider firstly, the reduction of error in the data, but also the capacity of the data to resolve the
593 magnetic structure of the solid earth without bias.

594 5.2.1 Phase-1

595 Point-by-point operations, in general, operate quickly on the data and are quite easily applied, so are
596 relatively low cost. The need to collate and reformat data from widespread sources, including
597 multiple base stations, and the magnetospheric components required for POMME is straightforward
598 but relatively time-consuming. There is also some overhead with the input and output of data to
599 external operations, such as POMME, in comparison to those that are integral to the data processing
600 package, such as the IGRF, although this is offset by the large degree of automation possible. The
601 POMME modelling itself is quite rapid, but may take some time for larger datasets. For example, in
602 our implementation for the 2016/2017 dataset, run in serial on a Linux Workstation, total
603 computation time was 40 minutes for ~266,000 datapoints (17,883 line km at 1 Hz sampling).

604 While it is essential to account for the secular magnetic field variation in a multi-year survey, we may
605 consider if the more complex POMME model provides a substantially more accurate correction than
606 the IGRF calculation. For the long-term base station records, comparison with the daily IGRF
607 correction shows that variability after POMME correction is reduced for all stations, with standard
608 deviations 1.2 to 2.1 nT lower ~ 2-5% of overall error. Although the bulk reduction on base station
609 signal variability is not marked in comparison to the IGRF correction (Fig. 4), the numerical difference
610 between POMME and IGRF is however not negligible. The overall differences between the full
611 POMME model and the IGRF model range from -57 nT to 256 nT, with a median magnitude of 38 nT,
612 and with substantial variations seen over a range of timescales, from annual to diurnal. For periods
613 shorter than 90 days, although POMME possesses much greater power spectral density than the
614 IGRF, it remains well below the power spectral density of the observatory-based records (Fig. 3),
615 however. 4D geomagnetic models such as POMME may become higher-powered, and higher
616 resolution, and there is scope for this approach to be more beneficial in the future, especially for
617 data in remote locations far from base stations.

618 For the base station correction, computation time is negligible, and the power spectral density is
619 comparable to the data down to periods of a few hours (Fig. 3). The multiple base station correction,
620 applied between bases over a long-term cycle with four bases and an inverse distance squared
621 scaling, is effective in the main, reducing the residual variability in the long-term base station
622 records, except at MAW. In comparison, running the same correction with values from only the
623 nearest base station yielded inferior results, with residual variability between 0.3 nT and 6 nT less in
624 the multi-base correction (1% to 14%). The value of the multi-base correction is variable, with strong
625 improvements for CSY, SBA and DRV, but weaker improvements for DMC, MAW and VOS where the
626 correction is highly dominated by a single station. With field data, located between the base
627 stations, the multiple-base-station correction process has a strong effect, reducing the cross-tie
628 errors substantially, by ~ 20% relative to the POMME corrected data.

629 Overall, the actions performed in phase-1 reduce variability in the long-term base station records,
630 with the largest proportional effect at SBA (reduced by 51%) and the weakest at DRV (17%).
631 Reduction in the cross-tie errors of the flight data is also substantial, with the mean reduced by 40%,
632 the median by 46% and the RMS by 36%. Substantial changes are made to the data, of the order of
633 tens to hundreds of nT. Our testing suggests that the level of error reduction is in all cases greater
634 than IGRF and single base station corrections, but perhaps not markedly so.

635 5.2.2 Phase-2

636 Phase-2 includes the geophysical inversion, which is used here to adjust the data to a constant
637 elevation, although other transforms are possible within the inversion algorithm including the
638 calculation of draped surveys, reduction to the pole and pseudogravity calculations. The data is

639 implicitly smoothed, due to the smoothness requirements of the inversion. Fourier-domain filtering
640 is commonly used to perform this continuation task, however alternatives such as equivalent point
641 source methods may also be used more effectively [Pilkington and Boulanger, 2017].

642 The inversion process is free from theoretical assumptions inherent to the frequency domain
643 approach, most notably the assumption that the potential field is evenly sampled on a plane (or line
644 in 2D), rather than a complexly shaped surface, however it is substantially more complex and time-
645 consuming than simple filtering. The inversion method is also superior to equivalent source methods
646 in that the recovered susceptibility distribution is smooth, has a depth extent and so can
647 accommodate dip, and involves off-profile magnetisation, albeit in a limited way. A stable mode of
648 downward continuation is enabled, although this will not generate new short-wavelength
649 information, except in the case of magnetisation of rough topography.

650 Our results show that the elevation adjustment generates notable improvement to the magnetic
651 data, with substantially stronger and more consistent definition of the anomalies beneath the thick
652 ice of interior Antarctica. In addition, while a direct reduction in cross-tie error was not seen, the
653 elevation adjusted data was superior to unadjusted data after levelling (Fig 5). Compared to the
654 corrected TMI, cross-tie errors in the elevation adjusted product were less by 12.4 nT for the RMS
655 (30%), 5.0 nT for the mean (26%), and 1.1 nT for the median (19%).

656 5.2.3 Phase-3

657 Despite the preceding adjustments, the data retain 4D characteristics, and the applied levelling
658 procedure is intended to be conservative, preserving the integrity of the individual lines, but
659 accounting for inconsistencies as identified by cross-tie errors. In terms of the impact on cross-tie
660 errors, the median-based line adjustment is substantial, accounting for ~ 30-35 % of the overall
661 cross-tie error reduction. While applying a base-level adjustment is a purely numerical adjustment, it
662 is a commonly accepted part of any data integration exercise, whether with grids or line data [Minty
663 *et al.*, 2003]. The cost of application is low, as the levelling algorithm runs in seconds. The main
664 advantage of the approach over typical approaches is that there is no requirement for a predefined
665 line order or hierarchy, nor the need for an operator to make decisions about which lines need
666 adjustment. While the median is a conservative choice, avoiding over-correction, it is in some cases
667 biased by an uneven distribution of intersections.

668 Spline interpolation, although a very common and robust interpolation procedure, has no physical
669 basis as a correction to magnetic data. Because it makes changes to the relative intensity of
670 anomalies along each line, the spline levelling should be applied only once cross-tie errors are
671 minimised. In our case the spline levelling is the smallest magnitude correction, in terms of nT, with
672 a mean magnitude of ~16-25 nT and a median magnitude of ~6 nT.

673 The final RMS cross-tie error following phase 3 is 41.5 nT for the corrected TMI and 29.1 for the
674 elevation adjusted data set; the means are 20.0 nT and 14.0 respectively, and the medians are 5.9 nT
675 and 4.8 nT.

676 5.3 Residual Errors

677 Following this data correction workflow, the magnitude of error reduction, as defined by cross-tie
678 errors is substantial. For the corrected TMI data, RMS error is reduced by 65%, with 79% reduction
679 of the mean error, and 92% reduction of the median error. For the elevation-adjusted data, greater
680 reductions are seen, by 76% (RMS), 85% (mean) and 93% (median), indicating the effect of the
681 elevation adjustment. Despite these reductions, absolute values of cross-tie errors remain above our
682 target precision of 3 nT. Residual errors are concentrated on several problematic lines, with residual

683 cross-tie errors also concentrated near the peaks or troughs of high amplitude anomalies, or at
684 regions of high gradient (Fig. 8). Further levelling may reconcile these errors, but the value of this
685 process may be limited, as the data retains residual 4D characteristics. For a greater reduction to
686 residual error, we may look more closely at improving our earlier corrections to the data, which are
687 systematically insufficient.

688 Phase 1 corrections are underpowered with respect to the signal they are intended to correct (Fig.
689 3). This situation may improve as geomagnetic models like POMME become higher-powered, in
690 particular for shorter periods, due to the inclusion of more detailed magnetic information [S. Maus
691 *et al.*, 2010]. The base station correction, which in this case relies on quite distant stations, often
692 with incomplete records, is inadequate with respect to removing diurnal and sub-diurnal intensity
693 variations (Fig 3). Besides having more closely spaced base-stations, which is infeasible,
694 improvement of the base-station correction may need a better approach to resolving four-
695 dimensional geomagnetic conditions from base station data.

696 Elevation differences are in principle accounted for by the inversion process, however, while
697 anomaly amplitudes are corrected, short-wavelength signals are missing in cases where the
698 elevation is adjusted downwards. Therefore, high-elevation lines, where they intersect low-elevation
699 lines, are not fully compatible, especially if the signal is rough at low elevations (Fig. 8). The inversion
700 process is also not uniformly precise and, where 3D anomalies are involved, the 2.5D model
701 structure may misrepresent the source geometry. Non-orthogonal strike and the effects of
702 remanent magnetisation are not fully accounted for.

703 **6 Conclusions**

704 Our workflow to process data seeks to correct for several systemic errors in magnetic data
705 correction that especially may have impact on sparse, four-dimensional surveys conducted across
706 multiple years in remote environments. The workflow includes three phases considering data as
707 individual points, lines and then sets of lines. With long-term base-station data we show that point-
708 by-point corrections are effective in reducing the variability of the signal by 25 to 50 %, with a similar
709 effect on reducing cross-tie errors at line intersections. These corrections are superior to a more
710 simple workflow, although the numerical error-reduction is not marked.

711 Phase 2 adjusts for differences in data-collection elevation, in this case adjusting all data to an
712 elevation of 2000 m, similar to the mean flight elevation of 2215 m. This step is effective in
713 increasing the relative amplitudes of anomalies in inland locations, where they are buried beneath
714 thick ice. A direct effect on cross-tie errors was not seen, however, the elevation adjusted data saw
715 much larger error-reductions in later levelling, indicating superior data consistency. Although
716 computationally intensive, the inversion process is superior to more simple approaches in that
717 anomalies can be reliably downward adjusted, with an inherently smooth and realistic model of
718 subsurface magnetisation.

719 Phase 3 constitutes the line-based levelling of the data, for which a median-based base-level
720 adjustment was highly effective in reducing cross-tie errors. Spline-levelling was less effective, but
721 reduced further the relatively small residual errors in the data. Leveling used a rapid semi-
722 automated approach, requiring little human intervention.

723 The final results of this workflow [A.R.A. Aitken and Nigro Rodrigues Alves Ramos, 2019], while still
724 not of comparable precision to tightly constrained HRAM datasets, reduced the initial errors by
725 between 76% to 93%, depending on metric. Confidence and interpretability is improved compared
726 to previous ICECAP data processing [A. R. A. Aitken *et al.*, 2014]. In particular, through elevation

727 adjustment, the data in inland regions is brought to a similar standard to the coastal regions and can
728 be interpreted without the systemic bias of flight altitude. This includes the use in automated
729 procedures, in particular those that depend on anomaly amplitudes, such as texture-mapping. The
730 improved data allow for new analysis to undertake more comprehensive tectonic and geological
731 research in the region.

732 **7 Acknowledgements**

733 This research was supported through the Australian Antarctic Science Program project grant 4460.
734 ICECAP and ICECAP-II data collection was supported through the Australian Antarctic Science
735 Program project grants 3103, 4077 and 4346. This work was supported by resources provided by the
736 Pawsey Supercomputing Centre with funding from the Australian Government and the Government
737 of Western Australia. The data presented in this work is available from the Australian Antarctic Data
738 centre (<http://dx.doi.org/doi:10.26179/5e015bb8dce7f>). Reviewers Fausto Ferraccioli and Tom
739 Jordan provided valuable comments.

740 **8 References**

741

742 Abraham, J., et al. (2008), Aeromagnetic Survey in Afghanistan: A Website for Distribution of Data,
743 *United States Geological Survey Open-file Report 2007-1247*.

744 Aitken, A. R. A., P. G. Betts, D. A. Young, D. D. Blankenship, J. L. Roberts, and M. J. Siegert (2016), The
745 Australo-Antarctic Columbia to Gondwana transition, *Gondwana Research*, 29(0), 136-152,
746 doi:<http://dx.doi.org/10.1016/j.gr.2014.10.019>.

747 Aitken, A. R. A., and L. Nigro Rodrigues Alves Ramos (2019), Reprocessed Magnetic Data from
748 ICECAP-I and ICECAP-II, 2008/2009 to 2016/2017, Ver. 1, edited, Australian Antarctic Data Centre,
749 doi:10.26179/5e015bb8dce7f.

750 Aitken, A. R. A., D. A. Young, F. Ferraccioli, P. G. Betts, J. S. Greenbaum, T. G. Richter, J. L. Roberts, D.
751 D. Blankenship, and M. J. Siegert (2014), The subglacial geology of Wilkes Land, East Antarctica,
752 *Geophysical Research Letters*, 2014GL059405, doi:10.1002/2014GL059405.

753 Behrendt, J. C., R. Saltus, D. Damaske, A. McCafferty, C. A. Finn, D. Blankenship, and R. E. Bell (1996),
754 Patterns of late Cenozoic volcanic and tectonic activity in the West Antarctic rift system revealed by
755 aeromagnetic surveys, *Tectonics*, 15(3), 660-676.

756 Behrendt, J. C., and C. S. Woterson (1970), Aeromagnetic and gravity investigations of the coastal
757 area and continental shelf of Liberia, West Africa, and their relation to Continental Drift, *Bulletin of*
758 *the Geological Society of America*, 81(12), 3563-3574, doi:10.1130/0016-
759 7606(1970)81[3563:AAGIOT]2.0.CO;2.

760 Blankenship, D. D., S. D. Kempf, and D. A. Young (2011, updated 2013), IceBridge Geometrics 823A
761 Cesium Magnetometer L2 Geolocated Magnetic Anomalies, Version 1, edited, NASA National Snow
762 and Ice Data Center Distributed Active Archive Center, Boulder, Colorado USA.,
763 doi:<http://dx.doi.org/10.5067/TO7WLC72UFAQ>.

764 Blankenship, D. D., S. D. Kempf, and D. A. Young (2012, updated 2013a), IceBridge HiCARS 2 L2
765 Geolocated Ice Thickness, Version 1, edited, NASA National Snow and Ice Data Center Distributed
766 Active Archive Center., Boulder, Colorado USA., doi: <http://dx.doi.org/10.5067/9EBR2TOVXUDG>.

767 Blankenship, D. D., S. D. Kempf, D. A. Young, J. L. Roberts, T. D. Van Ommen, R. Forsberg, M. J.
768 Siegert, S. J. Palmer, and J. A. Dowdeswell (2012, updated 2013b), IceBridge Riegl Laser Altimeter L2
769 Geolocated Surface Elevation Triplets, Version 1, edited, NASA National Snow and Ice Data Center

770 Distributed Active Archive Center. , Boulder, Colorado USA.,
771 doi:<http://dx.doi.org/10.5067/JV9DENETK13E>.

772 Carson, C. J., S. McLaren, J. L. Roberts, S. D. Boger, and D. D. Blankenship (2014), Hot rocks in a cold
773 place: High sub-glacial heat flow in East Antarctica, *Journal of the Geological Society*, 171(1), 9-12.

774 Chiappini, M., F. Ferraccioli, E. Bozzo, and D. Damaske (2002), Regional compilation and analysis of
775 aeromagnetic anomalies for the Transantarctic Mountains–Ross Sea sector of the Antarctic,
776 *Tectonophysics*, 347(1), 121-137, doi:[https://doi.org/10.1016/S0040-1951\(01\)00241-4](https://doi.org/10.1016/S0040-1951(01)00241-4).

777 Damaske, D. (1989), Geomagnetic activity and its implications for the aeromagnetic survey in North
778 Victoria Land, in *Geologisches Jahrbuch E38*, edited, pp. 41–58, Bundesanstalt für
779 Geowissenschaften und Rohstoffe, Hannover.

780 Ferraccioli, F., E. Armadillo, T. Jordan, E. Bozzo, and H. Corr (2009a), Aeromagnetic exploration over
781 the East Antarctic Ice Sheet: A new view of the Wilkes Subglacial Basin, *Tectonophysics*, 478(1-2), 62-
782 77.

783 Ferraccioli, F., E. Armadillo, A. Zunino, E. Bozzo, S. Rocchi, and P. Armienti (2009b), Magmatic and
784 tectonic patterns over the Northern Victoria Land sector of the Transantarctic Mountains from new
785 aeromagnetic imaging, *Tectonophysics*, 478(1-2), 43-61.

786 Ferraccioli, F., C. A. Finn, T. A. Jordan, R. E. Bell, L. M. Anderson, and D. Damaske (2011), East
787 Antarctic rifting triggers uplift of the Gamburtsev Mountains, *Nature*, 479(7373), 388-392.

788 Frederick, B. C., D. A. Young, D. D. Blankenship, T. G. Richter, S. D. Kempf, F. Ferraccioli, and M. J.
789 Siegert (2016), Distribution of subglacial sediments across the Wilkes Subglacial Basin, East
790 Antarctica, *Journal of Geophysical Research F: Earth Surface*, 121(4), 790-813,
791 doi:10.1002/2015jf003760.

792 Golynsky, A., et al. (2013), Air and shipborne magnetic surveys of the Antarctic into the 21st century,
793 *Tectonophysics*, 585, 3-12, doi:10.1016/j.tecto.2012.02.017.

794 Golynsky, A., et al. (2006), ADMAP — A Digital Magnetic Anomaly Map of the Antarctic, in
795 *Antarctica: Contributions to Global Earth Sciences*, edited by D. K. Fütterer, D. Damaske, G.
796 Kleinschmidt, H. Miller and F. Tessensohn, pp. 109-116, Springer Berlin Heidelberg, Berlin,
797 Heidelberg, doi:10.1007/3-540-32934-X_12.

798 Golynsky, A. V., et al. (2018), New Magnetic Anomaly Map of the Antarctic, *Geophysical Research*
799 *Letters*, 45(13), 6437-6449, doi:10.1029/2018gl078153.

800 Greenbaum, J. S., et al. (2015), Ocean access to a cavity beneath Totten Glacier in East Antarctica,
801 *Nature Geoscience*, 8(4), 294-298, doi:10.1038/ngeo2388.

802 Gross, L., C. Altinay, and S. Shaw (2015), Inversion of potential field data using the finite element
803 method on parallel computers, *Computers & Geosciences*, 84(Supplement C), 61-71,
804 doi:<https://doi.org/10.1016/j.cageo.2015.08.011>.

805 Hood, P. J., M. T. Holroyd, and P. H. McGrath (1979), Magnetic methods applied to base metal
806 exploration, in *Geophysics and Geochemistry in the Search for Metallic Ores*, edited by P. J. Hood, pp.
807 77-104, Geological Survey of Canada, Economic Geology Report 31.

808 Jordan, T. A., F. Ferraccioli, and P. T. Leat (2017), New geophysical compilations link crustal block
809 motion to Jurassic extension and strike-slip faulting in the Weddell Sea Rift System of West
810 Antarctica, *Gondwana Research*, 42, 29-48, doi:10.1016/j.gr.2016.09.009.

811 Kim, H. R., R. R. B. von Frese, P. T. Taylor, A. V. Golynsky, L. R. Gaya-Piqué, and F. Ferraccioli (2007),
812 Improved magnetic anomalies of the Antarctic lithosphere from satellite and near-surface data,
813 *Geophysical Journal International*, 171(1), 119-126, doi:10.1111/j.1365-246X.2007.03516.x.

814 King, J. H., and N. E. Papitashvili (2005), Solar wind spatial scales in and comparisons of hourly Wind
815 and ACE plasma and magnetic field data, *Journal of Geophysical Research: Space Physics*, 110(A2),
816 doi:10.1029/2004ja010649.

817 Lühr, H., and S. Maus (2010), Solar cycle dependence of quiet-time magnetospheric currents and a
818 model of their near-Earth magnetic fields, *Earth, Planets and Space*, 62(10), 14,
819 doi:10.5047/eps.2010.07.012.

820 Martos, Y. M., M. Catalan, T. A. Jordan, A. Golynsky, D. Golynsky, G. Eagles, and D. G. Vaughan
821 (2018), Heat flux distribution of Antarctica unveiled.

822 Maus, S., C. Manoj, J. Rauberg, I. Michaelis, and H. Lühr (2010), NOAA/NGDC candidate models for
823 the 11th generation International Geomagnetic Reference Field and the concurrent release of the
824 6th generation Pomme magnetic model, *Earth, Planets and Space*, 62(10), 729-735.

825 Maus, S., and P. Weidelt (2004), Separating the magnetospheric disturbance magnetic field into
826 external and transient internal contributions using a 1D conductivity model of the Earth, *Geophysical
827 Research Letters*, 31(12), doi:10.1029/2004gl020232.

828 Milligan, P., B. Minty, M. Richardson, and R. Franklin (2009), The Australia-wide airborne geophysical
829 survey - accurate continental magnetic coverage, *ASEG Extended Abstracts*, 2009(1), 1-9,
830 doi:<https://doi.org/10.1071/ASEG2009AB075>.

831 Minty, B. R. S., P. R. Milligan, A. P. J. Luyendyk, and T. Mackey (2003), Merging airborne magnetic
832 surveys into continental-scale compilations, *Geophysics*, 68(3), 988-995.

833 Morlighem, M. (2019.), MEaSURES BedMachine Antarctica, Version 1. Boulder, Colorado USA. NASA
834 National Snow and Ice Data Center Distributed Active Archive Center., edited,
835 doi:<https://doi.org/10.5067/C2GFER6PTOS4>. [Date Accessed].

836 Nabighian, M. N., V. J. S. Grauch, R. O. Hansen, T. R. LaFehr, Y. Li, J. W. Peirce, J. D. Phillips, and M. E.
837 Ruder (2005), The historical development of the magnetic method in exploration, *Geophysics*, 70(6),
838 33-61.

839 P. Welch (1967), The use of fast Fourier transform for the estimation of power spectra: A method
840 based on time averaging over short, modified periodograms in *IEEE Transactions on Audio and
841 Electroacoustics*, 15(2), 70-73.

842 Phillips, J. D. (1996), Potential-field continuation: Past practice vs. Modern methods, paper
843 presented at 1996 SEG Annual Meeting.

844 Pilkington, M., and O. Boulanger (2017), Potential field continuation between arbitrary surfaces —
845 Comparing methods, *GEOPHYSICS*, 82(3), J9-J25, doi:10.1190/geo2016-0210.1.

846 Rasmussen, R., and L. B. Pedersen (1979), End corrections in potential field modeling, *Geophysical
847 Prospecting*, 27(4), 749-760.

848 Reid, A. B. (1980), Aeromagnetic survey design, *Geophysics*, 45(5), 973-976.

849 Roberts, J. L., D. D. Blankenship, J. S. Greenbaum, L. H. Beem, S. D. Kempf, D. A. Young, T. D. Richter,
850 T. G. Van Ommen, and E. Le Meur (2018), EAGLE/ICECAP II GEOPHYSICAL OBSERVATIONS (SURFACE
851 AND BED ELEVATION, ICE THICKNESS, GRAVITY DISTURBANCE AND MAGNETIC ANOMALIES), Ver, 1,
852 edited, Australian Antarctic Data Centre, doi:<http://dx.doi.org/doi:10.26179/5bcfffdabcf92>.

853 Ruppel, A., J. Jacobs, G. Eagles, A. Läufer, and W. Jokat (2018), New geophysical data from a key
854 region in East Antarctica: Estimates for the spatial extent of the Tonian Oceanic Arc Super Terrane
855 (TOAST), *Gondwana Research*, 59, 97-107, doi:<https://doi.org/10.1016/j.gr.2018.02.019>.

856 Saltus, R. W., and R. P. Kucks (1995), Geomagnetic Activity and its Implications for the 1991–1992
857 Casertz Aeromagnetic Survey in Antarctica, in *Contributions to Antarctic Research IV*, edited, pp. 9-
858 17, doi:10.1002/9781118668207.ch2.

859 Tapping, K. F. (2013), The 10.7 cm solar radio flux (F10.7), *Space Weather*, 11(7), 394-406,
860 doi:10.1002/swe.20064.

861 Telford, W. M., L. P. Geldart, and R. E. Sheriff (1990), *Applied Geophysics Second Edition*, 770 pp.,
862 Cambridge University Press.

863 Thébault, E., et al. (2015), International Geomagnetic Reference Field: the 12th generation, *Earth*,
864 *Planets and Space*, 67(1), 79, doi:10.1186/s40623-015-0228-9.

865 Tinto, K. J., et al. (2019), Ross Ice Shelf response to climate driven by the tectonic imprint on seafloor
866 bathymetry, *Nature Geoscience*, 12(6), 441-449, doi:10.1038/s41561-019-0370-2.

867 Vine, F. J., and D. H. Matthews (1963), Magnetic anomalies over oceanic ridges, *Nature*, 199(4897),
868 947-949.

869 **9 Figure Captions**

870

871 Figure 1: ICECAP-I and ICECAP-II Data distribution by season. INTERMAGNET magnetic observatories
872 are indicated in green with IAGA codes and observatory names: CSY – Casey Station, DMC – Dome C,
873 DRV – Dumont d’Urville, MAW – Mawson, SBA – Scott Base, VOS – Vostok. Geomagnetic inclination
874 contours are in red. The ice-sheet and ice-shelf surface is from BedMachine Antarctica [Morlighem,
875 2019].

876 Figure 2: MDCWS-4D processing workflow. The workflow is divided into 3 main phases, each with
877 greater data connectivity.

878 Figure 3: Power Spectral Densities (PSDs) for the Scott Base observatory record (SBA) from
879 2008/07/01 to 2013/06/30, showing PSDs for the observed magnetic field intensity, the IGRF, the
880 POMME model with the magnetospheric components (full) and with default values for these (main).
881 Also shown is the base-to-base correction calculated for SBA from the other base stations. PSDs are
882 calculated with Welch’s method [P. Welch, 1967] using 1-minute data with a window size of 90 days.
883 IGRF data are calculated daily, so are not shown for frequencies above 0.5 per day.

884 Figure 4: Signal variability reductions for long-term observatory records with the applied point-by-
885 point corrections. Variability is expressed as the standard deviation of the entire long-term record,
886 from 2008/07/01 to 2013/06/30, in nT. Base-to-Base and IGRF corrections are not part of the base-
887 station processing workflow, but are shown to indicate the effectiveness of these.

888 Figure 5: Correction magnitudes (columns) and associated cross-tie error reductions (lines) for field
889 data. Cross-tie errors at line intersections are interpreted as indicating residual error.

890 Figure 6: Inversion setup for a single line. GL0211a is a coast-perpendicular line extending from Law
891 Dome inland towards the Aurora Subglacial Basin (location in Fig. 1). A) shows the whole line with
892 data location and subsurface masking. The surface of the ice sheet (grey line) is shown here but is
893 not part of the model. Source-sensor separation varies between ~ 1.5 km to almost 5 km. B) An
894 inset showing at fine scale the effective susceptibility scaling (k-scaling) of the model, with the mesh
895 superimposed. The region between the black and white lines delineates the transitional cells with
896 variable k-scaling. K-scaling is uniformly 1 beneath, and 0 above. Elements in this case are 50m high
897 and 82 m wide.

898 Figure 7: Data for ASB_JKB0a_GL0211a showing A) the corrected TMI data and the elevation
899 adjusted TMI at an elevation of 2 km. B) the elevation adjustment made to the data. C) The
900 susceptibility model, the elevations sampled and also the ice sheet surface and bed elevation, with
901 inset as in Fig 6.

902 Figure 8: Fully processed data, in A the corrected TMI; in B the elevation adjusted data at 2000m
903 elevation. In each case the left panel shows the overall dataset, while the insets on the right show a
904 zoomed in view of the western Wilkes Land (top) and the associated residual cross-tie errors
905 (bottom). All images use the same colour-scale. For other steps in the workflow, please refer to the
906 supporting information.

Figure 1.

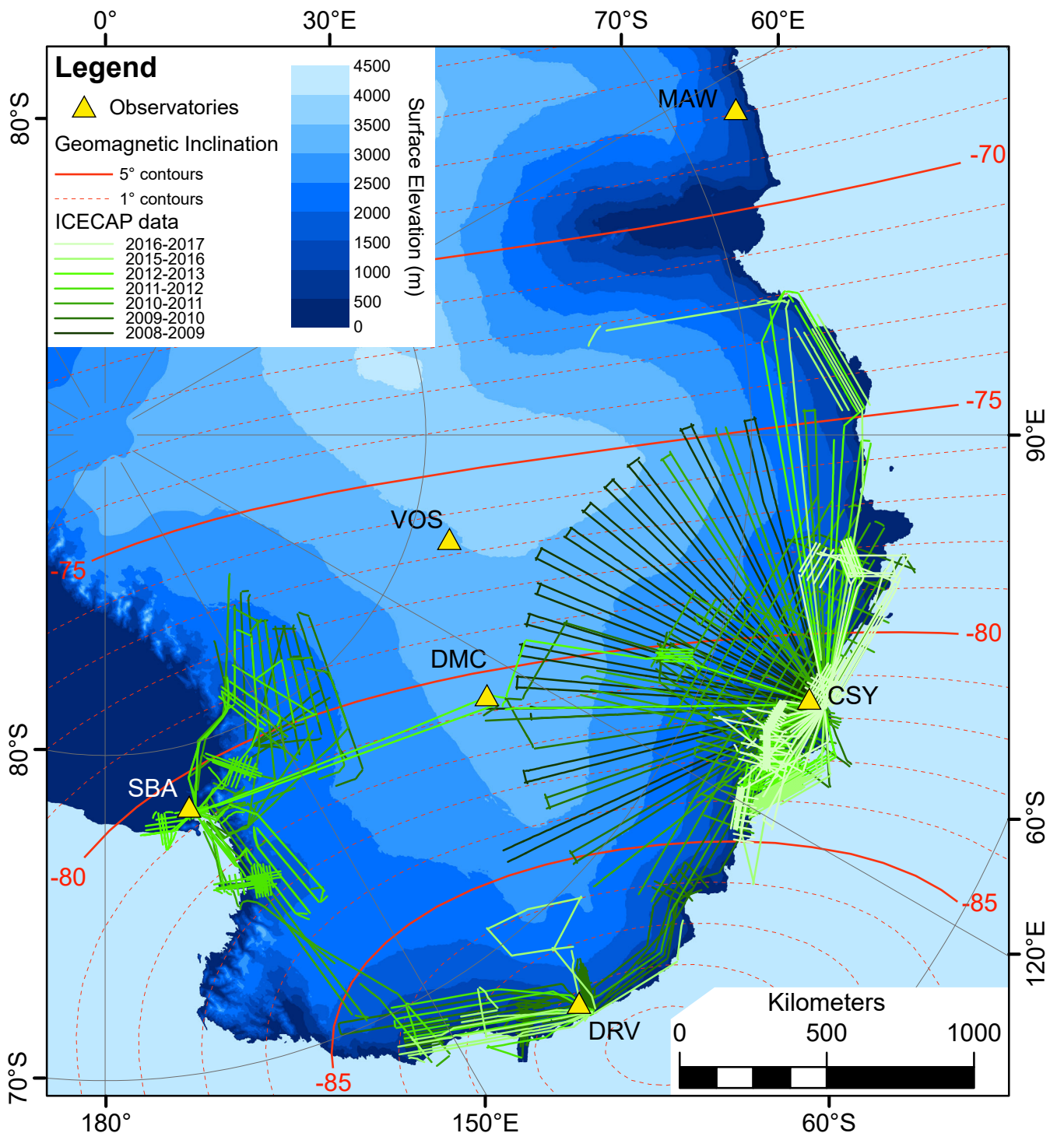


Figure 2.

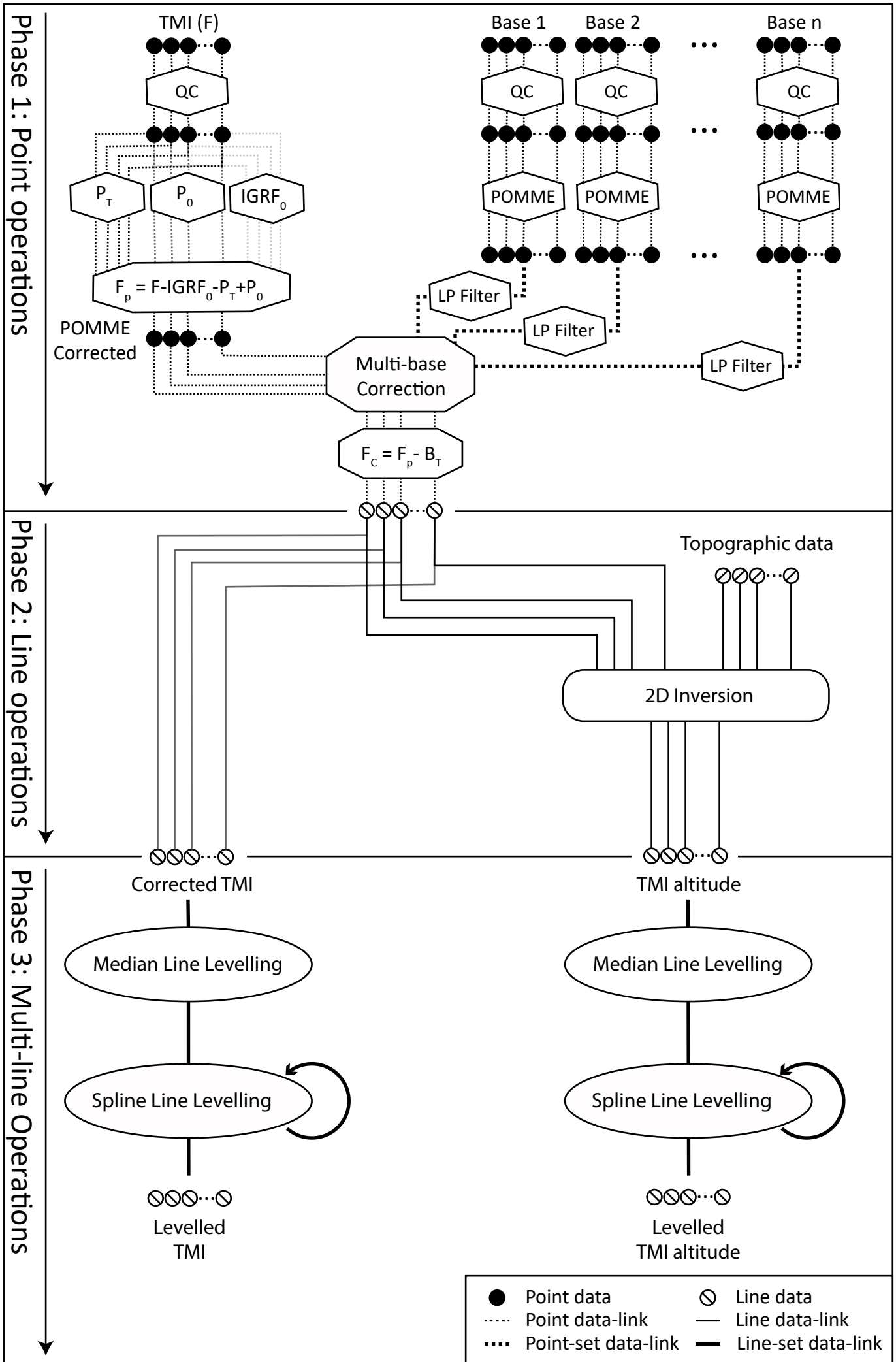


Figure 3.

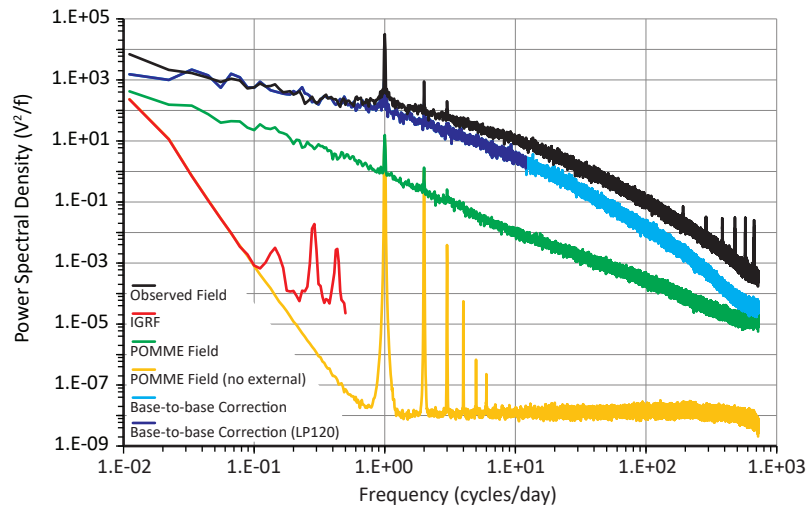


Figure 4.

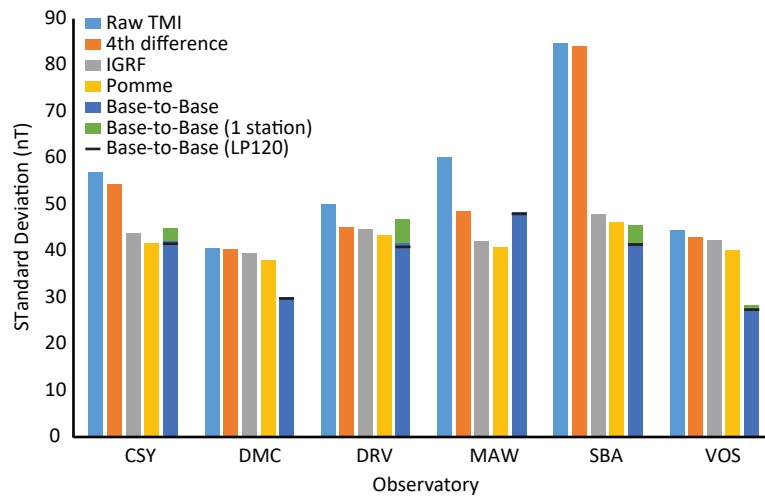


Figure 5.

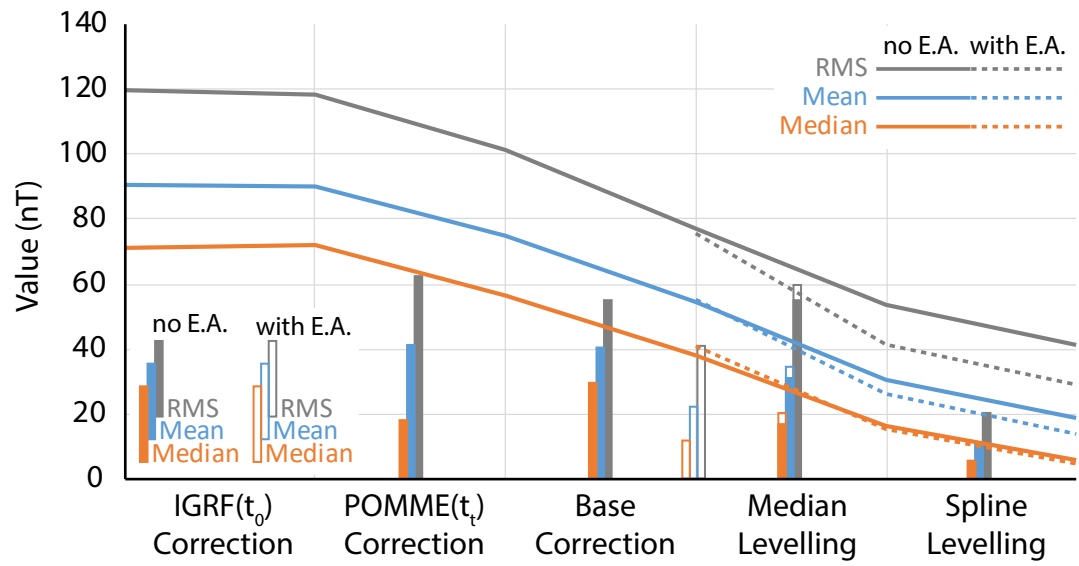


Figure 6.

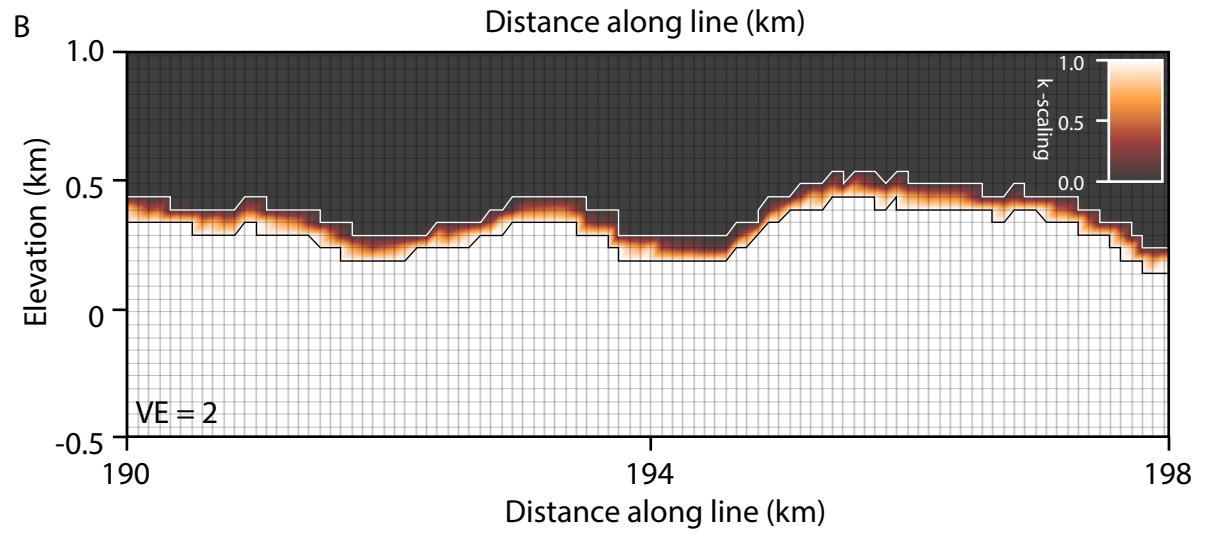
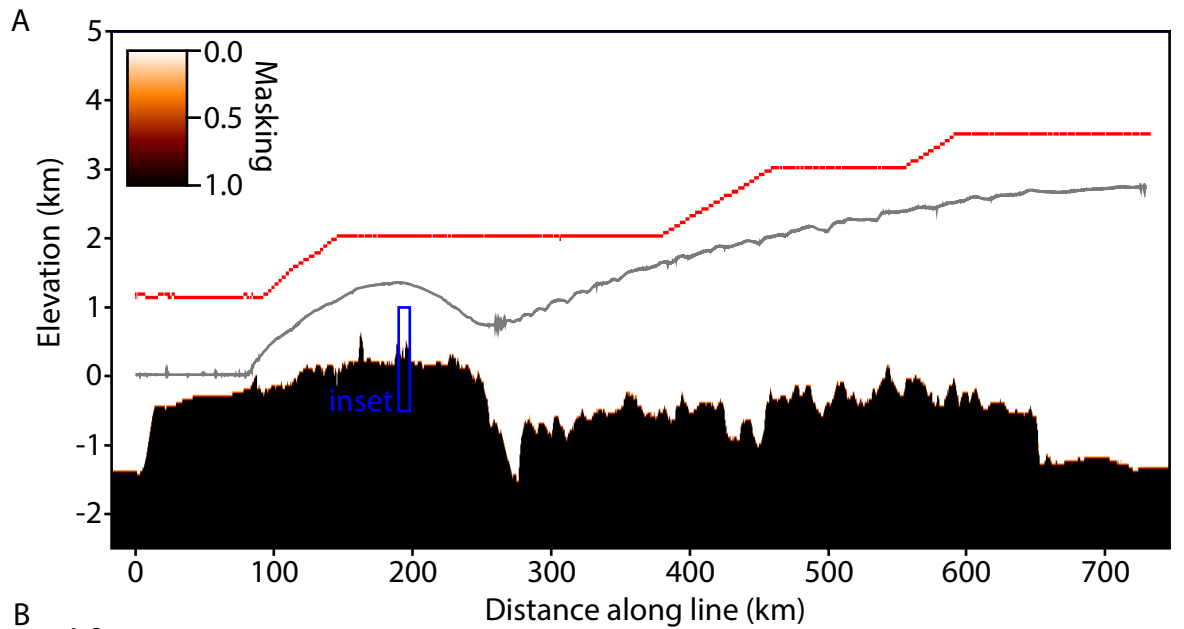


Figure 7.

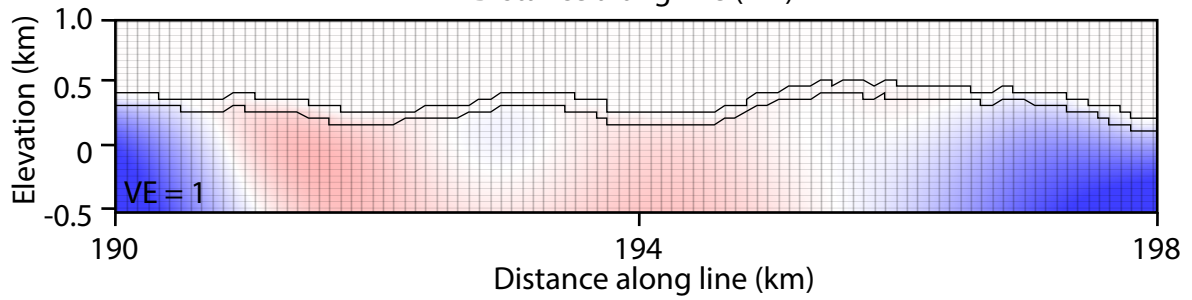
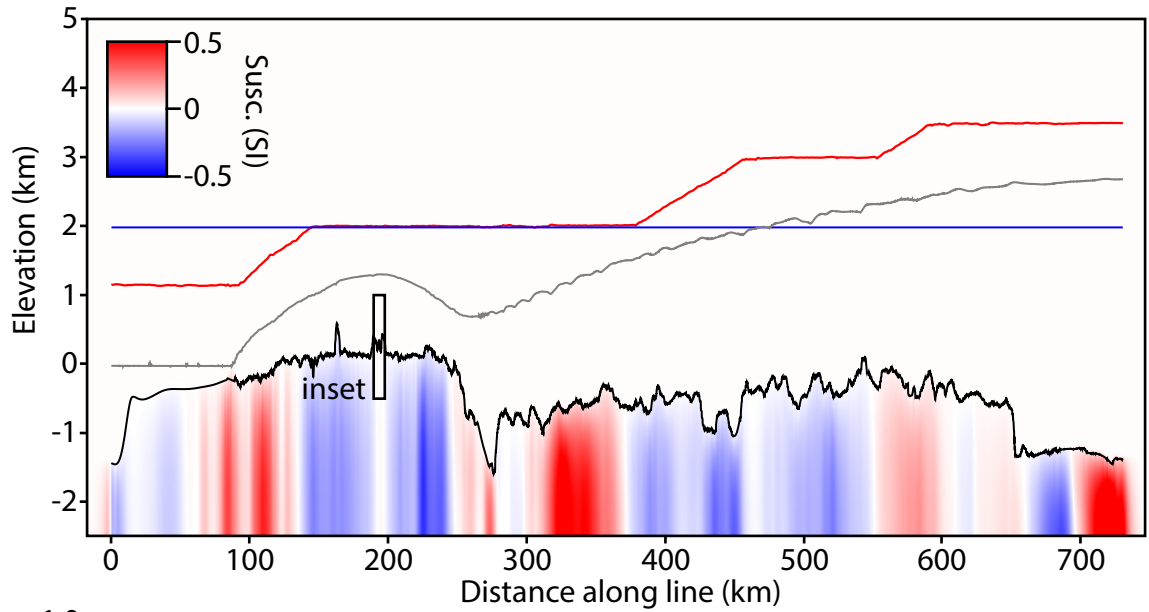
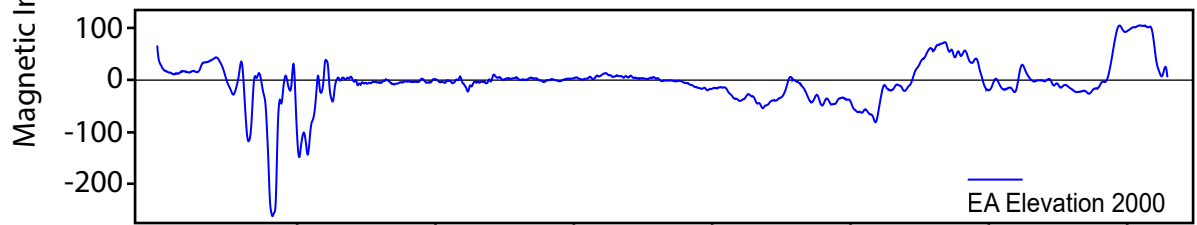
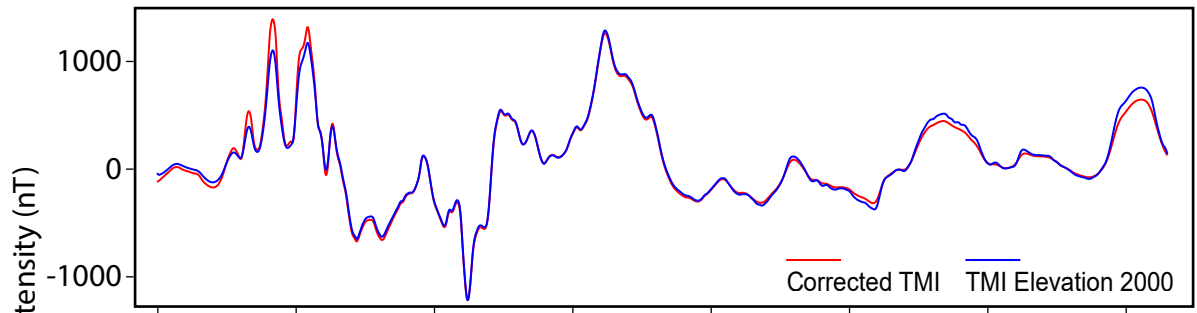


Figure 8.

